International Forum on Aeroelasticity and Structural Dynamics
IFASD 2024
17-21 June 2024, The Hague, The Netherlands

FLUTTER FLIGHT TESTING: USING OPERATIONAL MODAL ANALYSIS TO IDENTIFY, TRACK AND PREDICT FLUTTER FOR SAFE AND EFFICIENT FLIGHT TEST CAMPAIGNS

Keith Soal[1], Jan Schwochow[1], Robin Volkmar[1], Martin Tang[1], Carsten Thiem[1], Yves Govers[1], Marc Böswald[1], Thiemo Kier[2], Özge Süelözgen[2], Nicolas Guerin[3], Dániel Teubl[4], Julius Bartasevicius[4], Balint Vanek[5], Szabolcs Tóth[5], Mihály Nagy[5]

[1]German Aerospace Center DLR, Institute of Aeroelasticity
Bunsenstr. 10, 37073 Göttingen, Germany
keith.soal@dlr.de

[2]German Aerospace Center DLR, Institute for System Dynamics and Controll
Münchener Straße 20, 82234 Weßling, Germany

[3]The French Aerospace Lab ONERA, Aerodynamics Aeroelasticity Acoustics Department
29 avenue de la division Leclerc, F-92322 Chatillon, France

[4]Technical University of Munich TUM, the Chair of Aircraft Design
Boltzmannstrasse 15, 85748 Garching, Germany

[5]HUN-REN SZTAKI
Kende u. 13-17, 1111 Budapest, Hungary

Keywords: flutter flight testing, uav, structural dynamics, aeroelasticity, flipased

Abstract: Flutter flight testing is an important, challenging and safety critical part of aircraft flight envelope expansion. Since flutter is a complex phenomenon influenced by aerodynamics, structural dynamics, and control systems, understanding and modeling these interactions accurately can be difficult. Furthermore, the prediction of the flutter boundary is challenging (both numerically and in flight) due to the interaction of many variables such as airspeed, altitude, control surface positions, excitation amplitudes etc. The critical parameter for flutter monitoring is the aeroelastic damping. The damping also remains the most difficult parameter to identify and simulate accurately.

In order to demonstrate state-of-the-art testing, simulation and active control methods, a technology demonstrator was designed and built in the EU FLIPASED project. The UAV demonstrator with 7 m wing span and weighing 70 kg was designed to flutter in the achievable flight envelope. Ground Vibration Testing GVT was conducted, and the results were used to perform a flutter simulation. A flutter flight test campaign was then carried out with Operational Modal Analysis OMA running in real time on miniaturized hardware to identify and track the modal parameters. In this paper an overview of the flutter monitoring system will be presented, together with the simulation results and flutter flight test results. Finally, a comparison of the flight test and simulation results will be presented, together with the outlook of future work.

1 INTRODUCTION

Flutter monitoring remains a critical aspect of aerospace engineering due to the potentially catastrophic consequences of this aeroelastic phenomena. Flutter is a dynamic instability occurring when aerodynamic forces couple with structural vibrations, leading to oscillations that can rapidly increase and cause structural failure. Despite large research and development efforts in the field of structural dynamics and aeroelasticity, the identification and prediction of flutter in a flight experiment remain very challenging tasks. The main reason is the importance of accurate damping identification - the one parameter which still has largest uncertainties even for the most advanced algorithms.

Despite these challenges, flutter monitoring is crucial in the certification process of new aircraft. Improvements of identification methods, test procedures and simulations will therefore bring a major benefit to the aerospace sector. To this end, the EU-funded FLIPASED (Flight Phase Adaptive Aero-Servo-Elastic Aircraft Design Methods) project represents a state-of-the-art initiative aimed at coupling aeroelasticity, gust response, flight control methods, instrumentation and certification for future aircraft design. The consortium consists of the French Aerospace Lab ONERA, the Technical University of Munich TUM, the Institute for Computer Science and Control SZTAKI and the German Aerospace Center DLR. Each partner brought unique skills to the project including aircraft design and optimisation, aeroelastic tailoring, aircraft manufacturing, electronic design and manufacturing, simulation, flight test operations, Ground Vibration Testing GVT and Flight Vibration Testing FVT. The aircraft and consortium partners can be seen in Figure 1.

Figure 1: The P-FLEX aircraft and project consortium from ONERA, DLR, SZTAKI and TUM.

Figure 2: P-FLEX ready for take-off.

The Unmanned Aerial Vehicle UAV used as a technology demonstrator in this project is called P-FLEX. It weighs 70 kg, and has a 7 m wingspan. It is powered by a JetCat engine, has a V tail, and four control surfaces on each wing. The aircraft has three wing sets of identical shape and planform but different stiffness, and the flutter wing was flown in the flight test pertaining to this paper, see [1] for more details. The flutter wing was designed to flutter with a bending torsion coupling in the achievable flight envelope in order to demonstrate flutter identification as well as active control. The aircraft can be seen on the runway ready for take-off in Figure 2.

This paper will focus on the flutter flight test campaign. A GVT performed by ONERA and DLR was used to create a data driven modal model. This model was used to perform a flutter simulation. The first FVT data with the flight controller in open loop was also used to update the flutter predictions. Operational Modal Analysis OMA using the Stochastic Subspace Iden-

tification SSI was used to identify and track the modal parameters of the aircraft in real time. Both the simulation and OMA results were used to design the flight test plan for the closed loop tests and were crucial in achieving a successful flutter flight test campaign.

2 FLUTTER MONITORING SYSTEM

Due to the limited payload capacity of the UAV, a lightweight measurement system needed to be designed. The system requirements included: distributed sensors in the wing, fuselage and tail, it needed to be integrated in the Flight Control Computer FCC, it needed to perform signal processing, modal analysis and tracking in near real time, and needed a telemetry link to send data to a ground station. An overview of the developed flutter monitoring system can be seen in Figure 3.

The monitoring system was fully designed and built within the consortium. It consists of sixteen Inertial Measurement Units IMUs, designed by SZTAKI. These IMUs measured thirty acceleration signals in the wings, fuselage and V tail as seen in Figure 3. The data was sent using CAN bus to the FCC setup on a Raspberry pi 4. A lightweight messaging library called ZMQ was used to send the data in real time via a socket based communication channel to the Onboard Computer II OBCII via ethernet, see Figure 4. The OBCII was dedicated to running the flutter monitoring software, developed by DLR in Python. This software performed the signal processing, OMA and mode tracking. A data buffer of 40 seconds was used with a sliding window and therefore an update rate of 2 seconds. The modal parameters were then encrypted into an efficient data package, and sent via 433 MHz telemetry also programmed in Python using Finite State Machine FSM logic. Finally the data was received on the ground station, developed by TUM, decoded and displayed using the NASA OpenMCT GUI. Details about the embedded system development can be found in [2], the hardware in the loop testing in [3], the flight vibration testing of the aeroelastically stable wing in [4], and the flutter damping trends in [5].

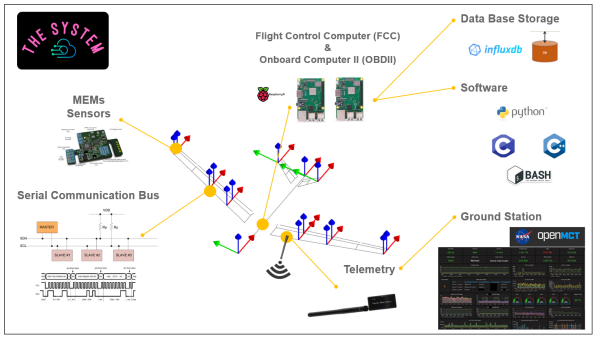

Figure 3: Flutter monitoring system architecture.

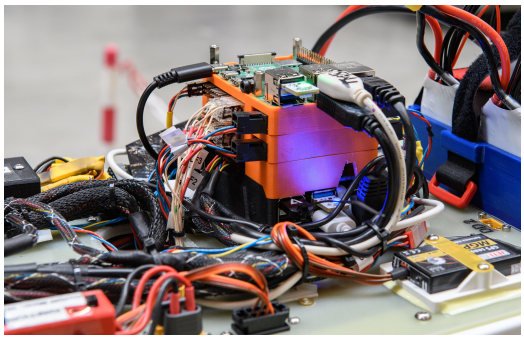

Figure 4: Flutter monitoring hardware including FCC and OBCII.

3 FLIGHT TEST CAMPAIGN

The flutter flight test campaign was conducted at the DLR Cochstedt flight test facility in 2023. The flight test team consisted of pilots and flight test engineers from TUM. Ground support regarding the FCC and baseline controller were provided by team members from SZTAKI. The active controller setup and deployment were done by DLR and SZTAKI. Simulations based on GVT and FVT were provided by ONERA and DLR. The flutter monitoring in flight was provided by DLR.

The relevant flight permits were obtained from the Luftfahrt-Bundesamt LBA in Germany. Based on the GVT and FVT results, flutter simulations were performed to determine the expected flutter speed. Flutter analysis using the finite element model indicated a flutter speed of 46 m/s with an anti-symmetric coupling. When changing from finite element model to modal model from GVT with some adjustments after open loop FVT, the predicted flutter speed changed to 56 m/s with a symmetric coupling. This estimate, together with low speed OMA test results were used to design the flutter flight test program as follows:

1. Open loop flights with constant bank angle circles from 44 to 52 m/s in 2 m/s increments.
2. Flight speed increments reduced to 1 m/s after 52 m/s until 54 m/s.
3. The aircraft should then land for offline validation of the results.
4. Closed loop flight to 61 m/s with DLR and then SZTAKI active controllers.
5. Open loop flight into flutter speed to confirm aeroelastic instability.

Figure 5: P-FLEX shortly after take-off.

Figure 6: P-FLEX in flight.

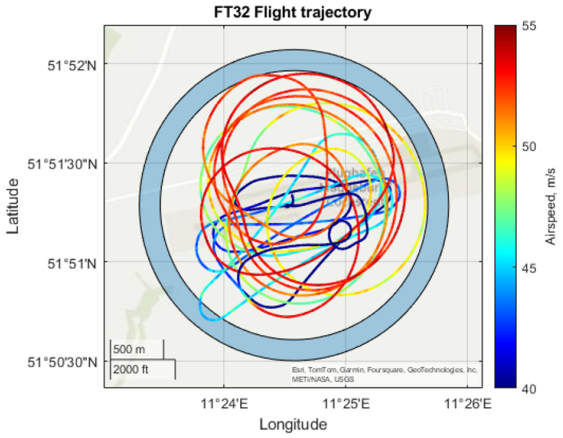

Figure 7: Flight track during FT32.

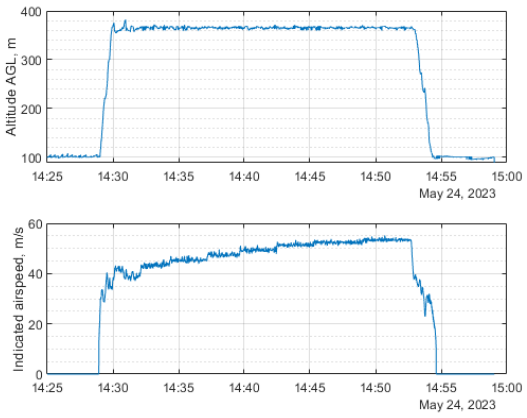

Figure 8: Flight profile: speed and altitude.

The P-FLEX aircraft can be seen after take-off and on a flight test point in Figures 5 and 6. It was found during the previous flight test campaigns that flying constant bank angle circles rather than horse race track patterns improved the stationarity of the data and time on test point, see [6] for further details. This provides more averages of the modal parameters which improve the certainty and also allow a statistical estimate of the uncertainties. The GPS coordinates of the constant bank angle circles within the visual range flight test box can be seen in Figure 7. The baseline controller was used with an augmented mode to help the pilots control the speed and altitude. The pilots could then focus on flying circles and remaining within the flight box. A

plot of the altitude 360 m AGL (height above ground) and the indicated airspeed can be seen in Figure 8. The speed is seen to be maintained with +- 1 m/s by the baseline controller, providing consistent data for the OMA algorithm.

4 SIMULATION MODEL

As a prerequisite for the FVT, it is required to measure the modal parameters of the airframe comprising eigenfrequencies, damping ratios and mode shapes in the course of a GVT. The modal parameters from the GVT are used to verify the numerical structural model, which is based on the Finite Element Method FEM. In case of accurate measurement of the modal mass, the experimental modal data set is used as a structural substitute model to be introduced in the flutter stability analysis. The vibrating structure induces aerodynamic loads, which act as additional stiffness, damping and mass and lag with respect to the oscillating deformation of the structure. For aeroelastic application in the subsonic domain, the well-known Doublet-Lattice Method DLM can provide the aerodynamic pressure loads in the frequency-domain [7], which can then be transformed to the time-domain using the rational polynomial fit [8]. In the case of a linear dynamic models with linear aerodynamics, one has the following system of ordinary differential equations:

$$[M]\{\ddot{u}\} + [C]\{\dot{u}\} + [K]\{u\} - q_\infty [Ae(\{\ddot{u}\}, \{\dot{u}\}, \{u\}, M_\infty)] = \{f(t)\} \tag{1}$$

where $[M]$, $[C]$ and $[K]$ are the mass, damping and stiffness matrices, respectively .The aerodynamic force matrix $[Ae]$ depends on the vector of nodal displacements $\{u\}$, nodal velocities $\{\dot{u}\}$, nodal acceleration $\{\ddot{u}\}$ and the Mach number M_∞. It is scaled with the dynamic pressure $q_\infty = \frac{1}{2}\rho_\infty V_\infty^2$ comprising atmospheric density ρ_∞ and the flight velocity V_∞ as true airspeed TAS. Eq. 1 can be projected onto the modal DOF, where the mode shapes ϕ_r are mass-normalized:

$$[I]\{\ddot{q}\} + \left[\backslash 2\zeta_r\omega_r\backslash\right]\{\dot{q}\} + \left(\left[\backslash\omega_r^2\backslash\right] - q_\infty[\Phi]^T[Ae][\Phi]\right)\{q\} = [\Phi]^T\{f(t)\} \tag{2}$$

where ω_r and ζ_r are the natrural frequencies and corresponding structural damping ratios, respectively. The modal DOF are coupled through the complex aerodynamic force matrix. The transformation of a time domain aerodynamic force impulse into the Laplace-Domain with Laplace variable $s = \sigma + i\omega$ reads

$$\begin{aligned}\mathcal{L}([Ae(t)]) &= \int_0^\infty [Ae(t)]\, e^{-st} dt \\ &\approx [Ae_0] + [Ae_1]\frac{b}{V_\infty}s + [Ae_2]\left(\frac{b}{V_\infty}s\right)^2 + \sum_{j=1}^{n_\gamma}[Ae_{2+j}]\frac{s}{s+\frac{V_\infty}{b}\gamma_j}\end{aligned} \tag{3}$$

For the rational approximation several real-valued lag-terms $\gamma_j = 1.7kr_{\max}\frac{j}{(n_\gamma+1)^2}$ must be introduced to represent the time delays between maximum deflection and aerodynamic force amplitudes. Since the DLM aerodynamic loads $[Q(ik)]$ are only dependent on reduced frequencies $k = \frac{\omega b}{V_\infty}$ for fixed geometry with reference chord b, Eq. 3 is usually transformed to perform the rational approximation:

$$[Q(ik)] \approx [\Phi]^T \left([Ae_0] + [Ae_1]\, ik - [Ae_2]\, k^2 + \sum_{j=1}^{n_\gamma} [Ae_{2+j}] \frac{ik}{ik + \gamma_j} \right) [\Phi] \tag{4}$$

The time-dependent external excitation forces $\{f(t)\}$ in Eq. (1) might be a combination of inertia and maneuver loads or pilot inputs. The output vector $\{y\,(t)\}$ contains the observable response of the aeroelastic system, which might be accelerations, velocities or even strains. The observation matrices$[Ca]$, $[Cv]$, $[Cd]$ connect the internal states and the output signals measured by a limited number of sensor types.

$$\{y\,(t)\} = [Ca]\,\{\ddot{u}\,(t)\} + [Cv]\,\{\dot{u}\,(t)\} + [Cd]\,\{u\,(t)\} \tag{5}$$

By simple mathematical manipulation, the aeroelastic model can be converted into a continuous-time state-space model:

$$\begin{array}{rl} \{\dot{x}\} = & [A_c] \cdot \{x\} + [B_c] \cdot \{f\,(t)\} \\ \{y\} = & [C] \cdot \{x\} + [D] \cdot \{f\,(t)\} \end{array} \tag{6}$$

where $\{x\}$ is the expanded state vector, where in addition to the structural states $\{x\}^T = \left\{\{u\}^T \{\dot{u}\}^T\right\}$, the aerodynamic lag-states $\{x_a\}$ from Eq. 3 are introduced:

$$\{x\} = \left\{ \begin{array}{c} \{u\} \\ \{\dot{u}\} \\ \{x_{a1}\} \\ \{x_{a2}\} \end{array} \right\} \tag{7}$$

The system matrix $[A_c]$ contains the time domain aeroelastic model:

$$[A_c] = \left[\begin{array}{cccc} 0 & [I] & 0 & 0 \\ -\left[\bar{M}\right]^{-1}\left[\bar{K}\right] & -\left[\bar{M}\right]^{-1}\left[\bar{C}\right] & q_\infty \left[\bar{M}\right]^{-1}[Ae_3] & q_\infty \left[\bar{M}\right]^{-1}[Ae_4] \\ 0 & [I] & -\left(\frac{V_\infty}{b}\right)\gamma_1\,[I] & 0 \\ 0 & [I] & 0 & -\left(\frac{V_\infty}{b}\right)\gamma_2\,[I] \end{array} \right] \tag{8}$$

with

$$\left[\bar{M}\right] = [M] - q_\infty\,[Ae_2]\left(\frac{b}{V_\infty}\right)^2, \quad \left[\bar{C}\right] = [C] - q_\infty\,[Ae_1]\left(\frac{b}{V_\infty}\right), \quad \left[\bar{K}\right] = [K] - q_\infty\,[Ae_0] \tag{9}$$

The detailed assembly of the aeroelastic system can be found in reference [9]. The modal parameters of the aeroelastic system comprise eigenfrequencies, damping ratios and modal participation factors, which can be calculated from the system matrices in Eq. 8. The eigenvalue decomposition of $[A_c(V_\infty, \rho_\infty)]$ leads to the diagonal matrix $[\Lambda]$ of discrete-time system poles λ_i and corresponding right eigenvectors $\{\psi\}_i$:

$$[A_c(V_\infty, \rho_\infty)]\,\{\psi\}_i = \lambda_i \{\psi\}_i \tag{10}$$

The damped eigenfrequencies f_i and damping ratios ζ_i can be calculated from the continuous-time system poles λ_i:

$$f_i(V_\infty, \rho_\infty) = \frac{\mathrm{Im}\left(\lambda_i(V_\infty, \rho_\infty)\right)}{2\pi}, \qquad \zeta_i(V_\infty, \rho_\infty) = -100\frac{\mathrm{Re}\left(\lambda_i(V_\infty, \rho_\infty)\right)}{|\lambda_i(V_\infty, \rho_\infty)|}. \tag{11}$$

Due to the relational approximation of the unsteady aerodynamic loads in Eq. 3, the p-method can be applied as direct solution and without $p-k$ iteration to match reduced frequencies from one speed step to the next.

Based on the modal GVT results, the experimental mode shapes are expanded to the DLM mesh to generate the harmonic aerodynamic loads in Eq. 3 for each mode at a given number of reduced frequencies. The DOF at the corner points of the aerodynamic boxes are interpolated from the limited number of measurement DOF by application of the volume spline method. Since not all 3D-spatial components are available at each support point, it is required to split the spline interpolation for each global direction. In Figure 9 and in Figure 10 the fundamental wing bending and the symmetrical wing torsion are plotted, respectively. All relevant modes shapes are listed in the Table 1.

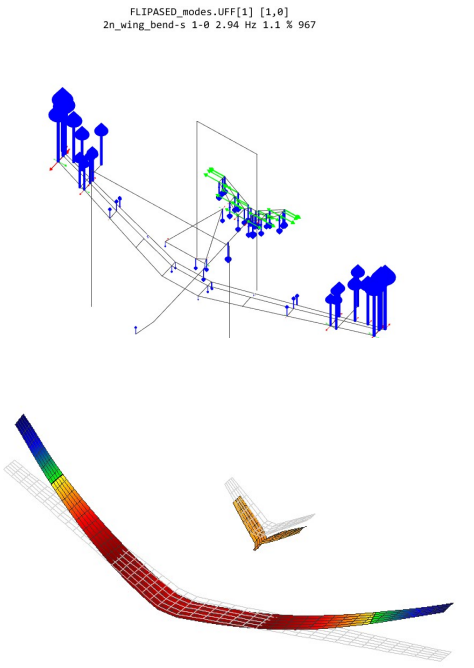

Figure 9: symmetric wing bending measured in GVT (green line in Figure 11 and 12).

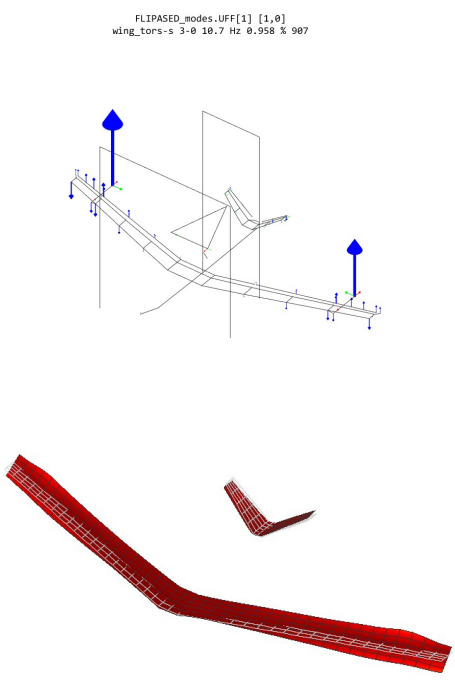

Figure 10: symmetric wing torsion measured in GVT (orange line in Figure 11 and 12).

In Figure 11 the frequencies over flight speed are plotted while in Figure 12 the corresponding dampings are shown. The flutter instability with lowest critical speed is caused by coupling of the modes rigid body pitch, 2n wing bending and symmetric wing torsion at 52 m/s. The

Table 1: Mode shapes used in flutter simulation

Mode	Description	f, Hz	g, %	Color in Fig. 11
1	rigid body fore-aft	0.00	0.00	
2	rigid body side	0.00	0.00	
3	rigid body heave	0.00	0.00	
4	rigid body roll	0.00	0.00	purple
5	rigid body pitch	0.00	0.00	blue
6	rigid body yaw	0.00	0.00	
7	2n wing bending	2.94	1.01	green
8	3n wing bending	7.22	0.80	orange
9	sym. wing torsion	10.74	0.96	light red
10	ant. wing torsion	11.16	1.08	dark red
11	4n wing bending	12.02	0.73	yellow

oscillating frequency is $f_{crit} = 7.96Hz$. Since the flutter equations are formulated as an LTI-system, it is an easy task to simulate the response in time domain. The continuous state-space model in Eq. 6 is discretized in time with fixed time intervals:

$$\left\{ \begin{array}{c} x_{k+1} \\ y_k \end{array} \right\} = \left[\begin{array}{cc} A_d & B_d \\ C & D \end{array} \right] \left\{ \begin{array}{c} x_k \\ u_k \end{array} \right\} \tag{12}$$

The zero-order hold assumption on the inputs $\{f\}_k$ yields the following relationship between the continuous-time and the discrete-time system:

$$[A_d] = e^{[A_c]\Delta t} \quad \text{and} \quad [B_d] = ([A_d] - [I])\,[A_c]^{-1}\,[B_c] \tag{13}$$

where Δt is the time increment of the dicretization. The response of the LTI-system due to vertical and lateral gust input is depicted in Figure 13 for the flight regime slightly below (left) and above (right) the critical flutter speed.

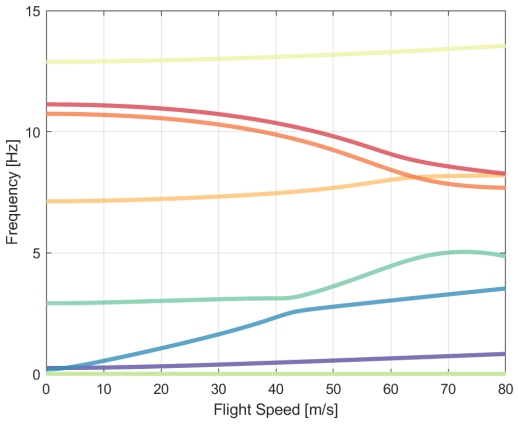

Figure 11: Frequencies over flight speed simulated with p-method.

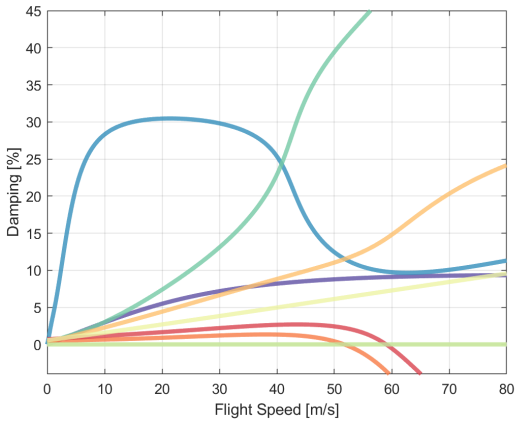

Figure 12: Damping over flight speed simulated with p-method.

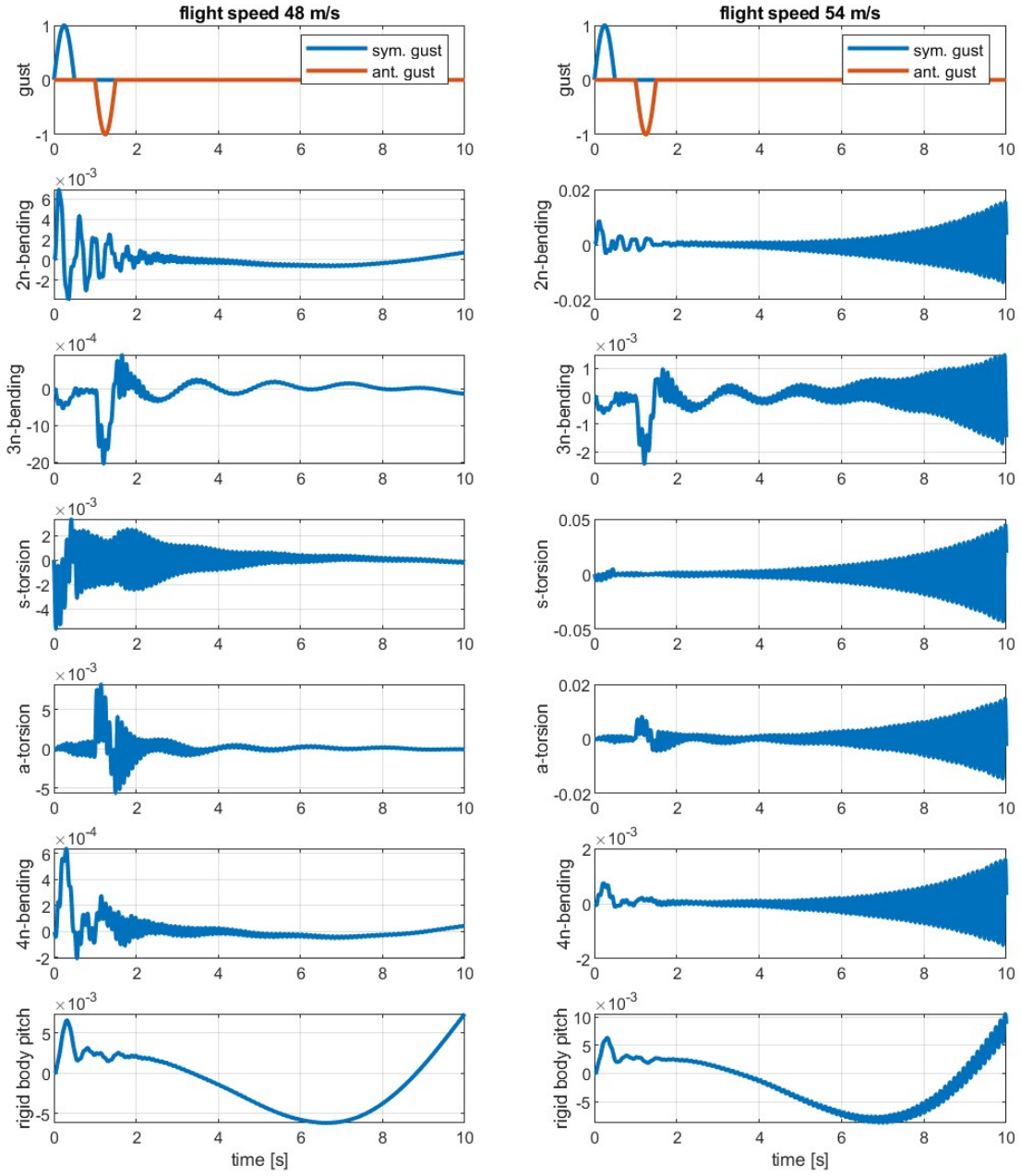

Figure 13: Simulated modal time response before and after critical flutter speed.

5 FLIGHT TEST OMA RESULTS

The modal parameters were identified in flight using OMA in the time domain with Stochastic Subspace Identification SSI. The DLR software was optimized to run in near real time in Python. A data buffer of 40 seconds was found to be long enough for accurate identification of both the frequency and damping ratio taking into account the excitation amplitude and signal to noise ratio of the sensors. The data buffer was also found to be short enough to contain nearly constant flight conditions in order to not smear or average the changes in frequency and damping as a function of flight speed. All OMA was performed using ambient excitation with no additional

excitation from control surfaces.

The SSI results of frequency and damping as a function of flight speed for open loop test points from 44 m/s to 54 m/s together with their uncertainties can be seen in Figures 14 and 15. Seven unique modes are identified and tracked between 0 Hz and 15 Hz. These include rigid body heave [purple], rigid body roll [blue], 2n wing bending [green], 3n wing bending [orange], symmetric wing torsion [light red], anti-symmetric wing torsion [dark red], 4n wing bending [yellow]. The corresponding mode shapes are shown in Figures 22 to 29 in the Appendix. The aeroelastic damping of the 2n wing bending mode in green was measured around 30 %. The aeroelastic damping of the rigid body modes were highly damped above 40 %. The aeroelastic damping of the other elastic modes were measured below 10 %.

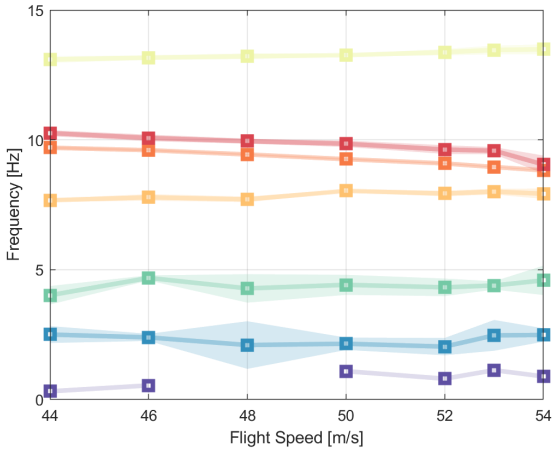

Figure 14: Frequency vs flight speed identified by SSI.

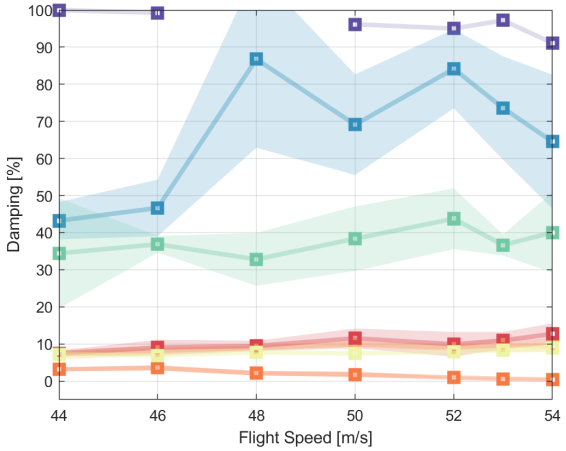

Figure 15: Damping vs flight speed identified by SSI.

By zooming in on the damping below 20 %, see Figure 16, it can be seen that the damping of the symmetric wing torsion [light red] decreases from 3.3 % at 44 m/s to 0.4 % at 54 m/s. This indicated that the symmetric wing torsion was very close to becoming unstable. Furthermore, the coupling can be seen to occur between the 2n wing bending mode which increases in frequency and damping and the symmetric wing torsion mode which decreases in frequency and damping. It can also be seen that the uncertainty in the damping decreases towards the flutter boundary. This is due to the high level of excitation, resulting in well identified modal parameters.

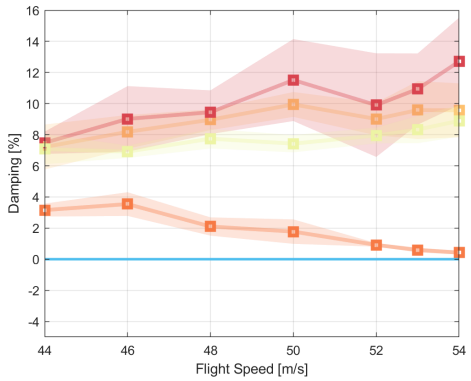

Figure 16: Damping ratios of flutter critical modes.

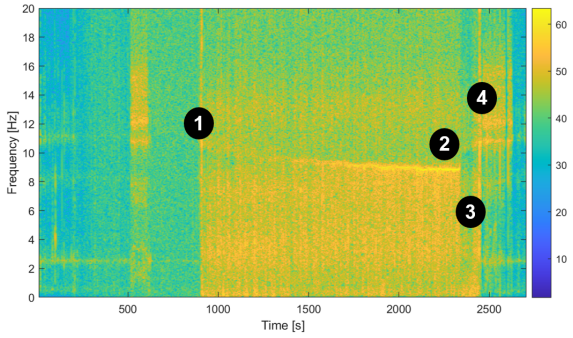

Figure 17: Spectrogram +Z: left hand wing tip.

The spectrogram of the +Z sensor in the leading edge wing tip of the left wing can be seen in Figure 17. At around 1000 seconds (Point 1) the aircraft takes off. From around 1500 seconds to 2400 seconds (Point 2) a bright line appears at approximately 9.7 Hz and decreases in frequency with increasing flight speed to 8.7 Hz. The symmetric wing torsion mode is therefore seen to be dominant as the aircraft approaches the flutter instability. Shortly thereafter the aircraft reduces speed (Point 3) and the dominant symmetric torsion mode disappears. The aircraft then lands at Point 4.

6 FLIGHT TEST OMA RESULTS VS SIMULATION MODEL

The results of the simulation model can then be compared to those measured in flight during the flutter test. In this comparison the first seven modes are included. The damped natural frequencies are plotted over the speed range 0 to 80 m/s in Figure 18. The damping ratios are compared over the same speed range in Figure 19. The solid lines show the simulated results with the p-method, and the squares show the in-flight modal parameters, with associated uncertainties. The frequencies and damping ratios show good agreement between the simulation and measured results. The trends of decreasing frequency and damping for the symmetric torsion mode (light red) is the most important parameter for the flutter stability and shows very good agreement.

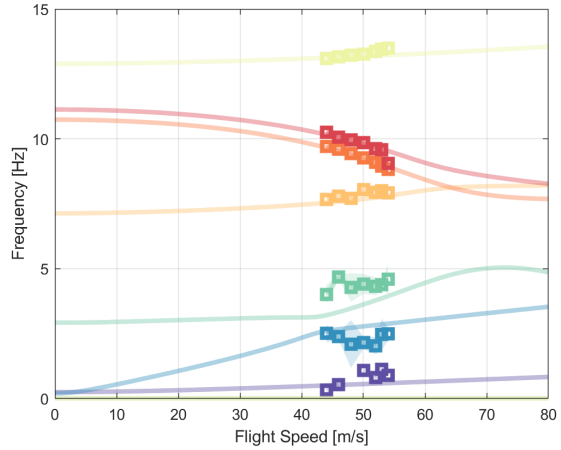

Figure 18: Frequencies over flight speed simulated with p-method and FVT results.

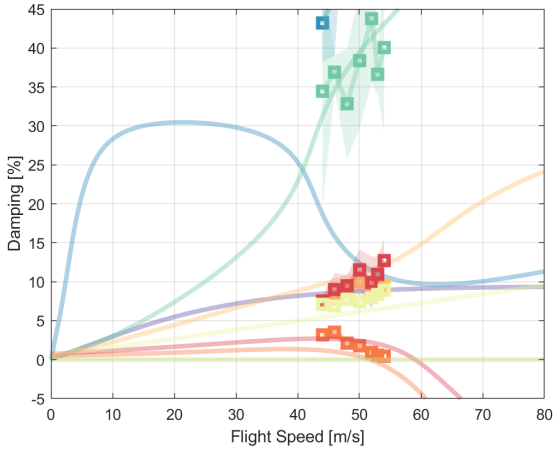

Figure 19: Dampings flight speed simulated with p-method and FVT results.

By zooming in on the speed range between 42 m/s and 56 m/s one can compare more closely the results in the flight test envelope, see Figures 20 and 21. Here it can be seen that damped natural frequencies of heave [purple], roll [blue], 3n wing bending [orange], symmetric torsion [light red], ant-symmetric torsion [dark red] and 4n wing bending [yellow] fit extremely well, and follow the same trajectory as a function of flight speed. A systematic deviation is however observed in the 2n wing bending frequency which needs to be investigated in further detail. The correlation of the damping is slightly worse between measurement and simulation. Nevertheless, the 2n wing bending shows good agreement with increasing damping from approximately 30 % to 40 %. The symmetric wing torsion mode also agrees well with a decrease from approx 3-4 % to under 0.5 %. The flutter simulation predicts a flutter speed of 52 m/s after updating while the in flight results measured 0.4 % damping at 54 m/s and therefore predicted flutter to occur between 56 - 58 m/s based on an interpolation of the damping.

After successfully demonstrating active control and flying through the flutter speed in close

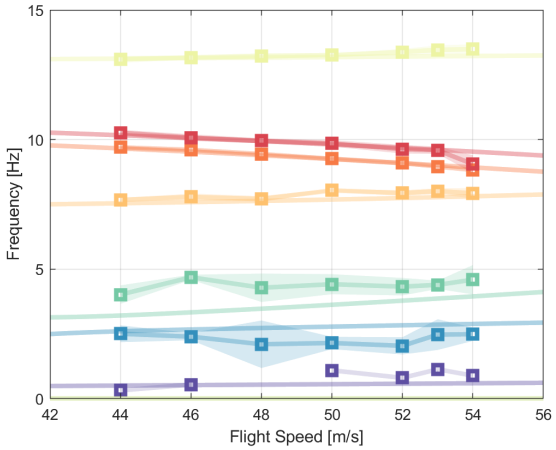

Figure 20: Frequencies over flight speed simulated with p-method and FVT results.

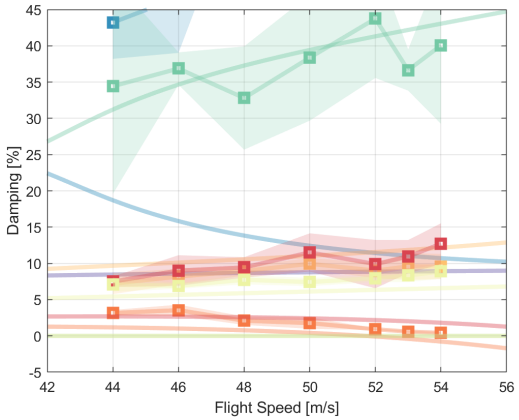

Figure 21: Dampings flight speed simulated with p-method and FVT results.

loop, which is the topic of other research from SZTAKI and DLR, the aircraft was flown towards the predicted flutter speed in open loop. The goal of this penultimate flight of the FLIPASED project was to prove whether a flutter instability indeed existed. Unfortunately the weather conditions during the final flight test were very turbulent, and therefore it was difficult to maintain the airspeed within +-3 m/s. Nevertheless while approaching 56 m/s the wings experienced large oscillations resulting in structural damage and finally partial loss of the flutter break system. Whether the instability reached a Limit Cycle Oscillation LCO or was structurally damaged during exponential increase in vibration is still an open question. What is however clear, is that an aeroelastic flutter instability was experienced in flight, in the region were is was predicted from both measurements and simulations.

7 CONCLUSION

A successful flutter flight test campaign was completed during the final week of testing in the FLIPASED project. The GVT and FVT created the foundations for accurate numerical simulations of the flutter speed and flutter mechanism. The simulation model predicted a symmetric flutter coupling between the 2n wing bending mode and the symmetric torsion mode to become unstable at 52 m/s. The flutter monitoring system was able to identify and track the modal parameters in-flight using OMA algorithms in near real time. Results from the simulations and flight testing were used to design and conduct an efficient and safe flutter flight test campaign. During the flight test campaign it was confirmed from in flight measurements that the damping of the symmetric wing torsion mode decreased from 3.3 % at 44 m/s to 0.4 % at 54 m/s. Finally the aircraft was flown to the flutter speed in open loop where it was damaged due to dynamic flutter instability. Thus confirming the reliability of the in flight monitoring system and simulations.

8 OUTLOOK

Future work will be focused on two main topics: [1] the quantification of the effectiveness of the active controllers using OMA. [2] feeding the system matrices (A,B,C,D) back to the controller for semi-active flutter control using damping estimates instead of measured responses. Finally as part of the open data initiative all flight test data is openly available [10] for future benchmarking of new methods and collaboration with new partners.

9 REFERENCES

[1] Sodja, J., De Breuker, R., Meddaikar, Y. M., et al. (2020). Ground testing of the flexop demonstrator aircraft. In *AIAA Scitech 2020 Forum*. p. 1968.

[2] Soal, K., Thiem, C., Meier, T., et al. (2022). Embedded flight vibration testing system for online flutter monitoring of uavs. In *19th International Forum on Aeroelasticity and Structural Dynamics, IFASD 2022*.

[3] Soal, K., Nagy, M., Teubl, D., et al. (2022). Hardware-in-the-loop testing of a miniaturized real time flutter monitoring system for uavs.

[4] Soal, K., Volkmar, R., Thiem, C., et al. (2023). Flight vibration testing of the t-flex uav using online modal analysis. In *AIAA SCITECH 2023 Forum*. p. 0373.

[5] Soal, K., Volkmar, R., Thiem, C., et al. (2024). Identification of the flutter boundary during flight testing using operational modal analysis. In *10th International Operational Modal Analysis Conference, IOMAC 2024*.

[6] Bartasevicius, J., Teubl, D., Thomas, S., et al. (2024). Lessons learned from flight testing active flutter suppresion technologies. In *International Forum on Aeroelasticity and Structural Dynamics, IFASD 2024*.

[7] Albano, E. and Rodden, W. (1969). A doublet-lattice method for calculating lift distributions on oscillating surfaces in subsonic flows. *Journal of Aircraft*, 7(2), 279–285.

[8] Roger, K. (1977). Airplane math modeling methods for active control design. Tech. Rep. AGARD-CP-228, AGARD.

[9] Botez, e. a., R.M. (2003). Method for flutter aero-servoelastic open loop analysis. *Canadian Aeronautics and Space Journal*, 49(4), 179–190.

[10] Bartasevicius, J., Teubl, D., Seren, T., et al. (2023). FliPASED Flight test data. doi: 21.15109/CONCORDA/PU4R32.

COPYRIGHT STATEMENT

ACKNOWLEDGMENTS

The work presented has been conducted within the framework of projects FLEXOP (grant agreement No. 636307) and FLiPASED (grant agreement No. 815058) funded from the European Union's Horizon 2020 research and innovation program.

10 APPENDIX

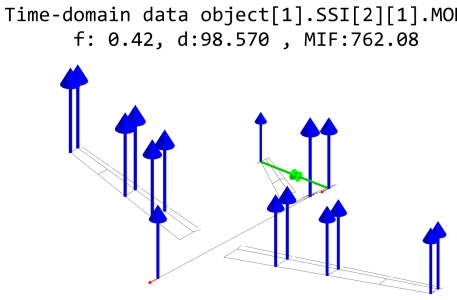

Figure 22: a/c heave.

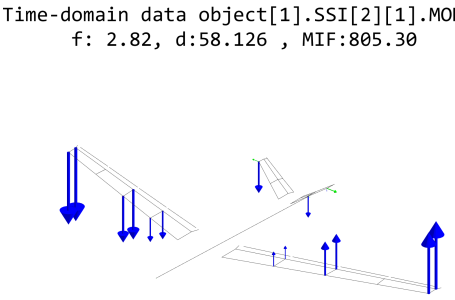

Figure 23: a/c roll.

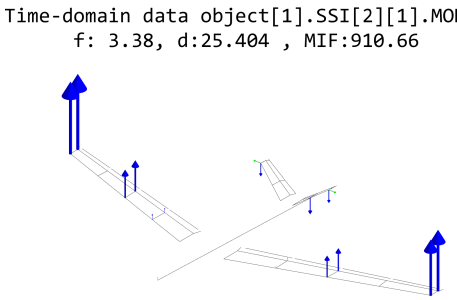

Figure 24: 2n wing bending.

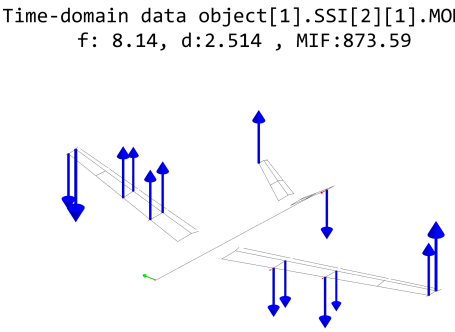

Figure 25: 3n wing bending.

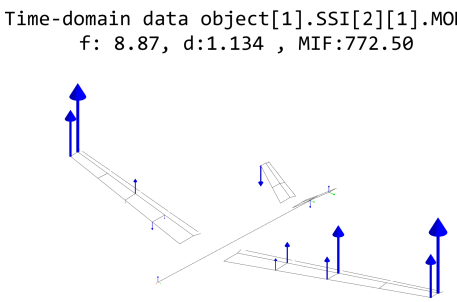

Figure 26: symmetric wing torsion.

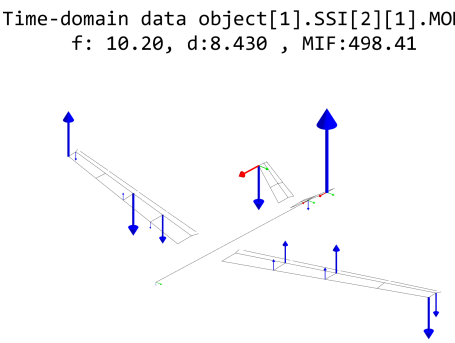

Figure 27: anti-symmetric wing torsion.

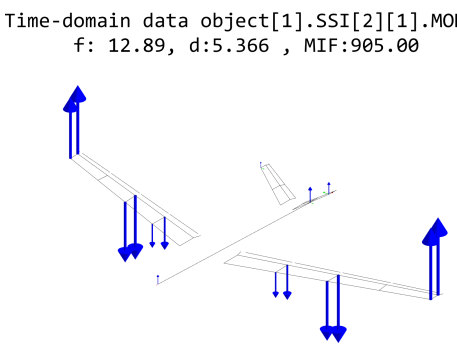

Figure 28: 4n wing bending.

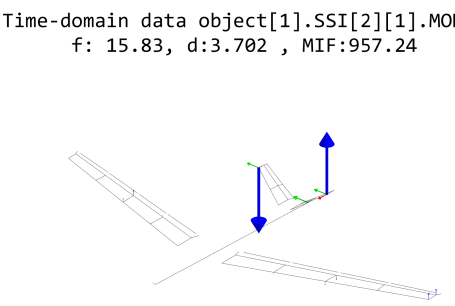

Figure 29: V-tail roll.